




Article

# High Strain Rate Deformation Behavior of Gradient Rolling AZ31 Alloys

Yingjie Li <sup>1</sup>, Hui Yu <sup>1,\*</sup>, Chao Liu <sup>1</sup>, Yu Liu <sup>2</sup>, Wei Yu <sup>3</sup> , Yuling Xu <sup>4</sup>, Binan Jiang <sup>5</sup>, Kwangseon Shin <sup>6</sup>   
and Fuxing Yin <sup>7,\*</sup> 

- <sup>1</sup> Tianjin Key Laboratory of Materials Laminating Fabrication and Interfacial Controlling Technology, School of Materials Science and Engineering, Hebei University of Technology, Tianjin 300130, China; a2323496328@163.com (Y.L.); sk8liuchao@163.com (C.L.)
- <sup>2</sup> School of Materials Science and Engineering, Hunan University, Changsha 410082, China; lyahaqhn@163.com
- <sup>3</sup> School of Materials Science and Engineering, Hefei University of Technology, Hefei 200039, China; yuwei52213@163.com
- <sup>4</sup> Baosteel Metal Co., Ltd., Shanghai 200940, China; xuyuling@baosteel.com
- <sup>5</sup> PLA Army Academy of Artillery and Air Defense, Hefei 230031, China; tata\_maxwell@163.com
- <sup>6</sup> Department of Materials Science and Engineering, Seoul National University, Seoul 08826, Republic of Korea; ksshin@snu.ac.kr
- <sup>7</sup> Institute of New Materials, Guangdong Academy of Science, Guangzhou 510651, China
- \* Correspondence: huiyu@vip.126.com (H.Y.); yinfuxing@hebut.edu.cn (F.Y.)

**Abstract:** A dynamic impact test was performed on as-rolled AZ31 alloys with gradient microstructure under various strains. The microstructural evolution and mechanical properties were systematically investigated. As the strain rate gradually increased, an increasing number of twins were formed, facilitating dynamic recrystallization (DRX), and the mechanical properties were also gradually improved. The microstructure became heterogeneous at higher strain rates, but the peak stress decreased. The impact process resulted in a significantly higher performance due to microstructural refinement, work hardening by dislocations, and precipitates. In addition, both the adiabatic shear band and the adjacent crack experienced a temperature rise that exceeded the recrystallization temperature of the alloys. This observation also explains the presence of ultrafine recrystallized grains within the adiabatic shear band and the appearance of molten metal around the crack.

**Keywords:** AZ31; high strain rate; gradient rolling; microstructure; mechanical property



**Citation:** Li, Y.; Yu, H.; Liu, C.; Liu, Y.; Yu, W.; Xu, Y.; Jiang, B.; Shin, K.; Yin, F. High Strain Rate Deformation Behavior of Gradient Rolling AZ31 Alloys. *Metals* **2024**, *14*, 788. <https://doi.org/10.3390/met14070788>

Academic Editor: Zbigniew Pater

Received: 20 May 2024

Revised: 30 June 2024

Accepted: 2 July 2024

Published: 5 July 2024



**Copyright:** © 2024 by the authors. Licensee MDPI, Basel, Switzerland. This article is an open access article distributed under the terms and conditions of the Creative Commons Attribution (CC BY) license (<https://creativecommons.org/licenses/by/4.0/>).

## 1. Introduction

Magnesium (Mg) is recognized as the fourth most abundant metal worldwide. Its lightweight nature, combined with its enhanced strength and processing capabilities, has led to the widespread utilization of Mg alloys across various industries such as aviation, automobiles, electronics, and medicine [1–5]. Particularly in the case of aerospace and automotive applications, magnesium alloys often experience dynamic loading, including impact, collision, and explosion, which necessitates the need to characterize and improve the mechanical properties of magnesium alloys at high strain rates. Typically, wrought Mg alloys manufactured by extrusion and rolling processes demonstrate superior properties [6–10], and they also result in a distinct fiber texture, leading to noticeable anisotropy [11–14]. However, the experimental samples are small in size, and only a single microstructure can generally be formed after plastic deformation, while the actual magnesium alloy forgings lack a uniform microstructure due to the different degrees of deformation in each part. Gradient rolling can produce samples with different deformation degrees at the same time, thus greatly reducing the test cost and experimental error [15].

Recently, the majority of research efforts on the deformation behavior of Mg alloys have primarily focused on quasi-static conditions, with fewer investigations into high strain rate deformation behavior [16]. In general, the deformation mechanism may be altered

under high strain rate compression compared to quasi-static compression [17–19]. Thus, exploring the microstructural evolution of Mg alloys under high strain rates would play a crucial role in understanding such a phenomenon, which, in turn, would allow for a better understanding of related mechanical properties [20–25]. For instance, Yu et al. [26] conducted dynamic impact tests on the EW75 Mg alloy, demonstrating that an increase in strain rate correspondingly led to a higher number of twins and recrystallized grains, which resulted in improved mechanical properties. Moreover, Ji et al. [27] observed a diminishing basal texture trend in the edge and central regions of a Mg alloy using the cross-rolling process.

However, the existing literature primarily focuses on individual processing and lacks systematic experiments on the high strain rate deformation behavior of magnesium alloys. Therefore, this study aims to bridge this research gap by conducting dynamic impact tests on AZ31 Mg alloys. All specimens underwent varying levels of deformation and were exposed to different strain rates. The main objective was to investigate how high strain rates influence the mechanical properties and microstructural evolution of gradient-deformed Mg alloys. The findings will not only contribute to a theoretical foundation but will also provide technical insight for developing high performance Mg alloys used in dynamic load conditions.

## 2. Experimental Section

A commercial AZ31 (Mg-3.25Al-0.92Zn-0.34Mn, wt.%) Mg alloy (provided by Dongguan Kuangyu Metal Materials Co., Ltd., Dongguan, China) with a diameter of 60 mm and a height of 120 mm was used. The specimen was extruded and deformed into a cylindrical bar with a diameter of 20 mm, then turned into a conical workpiece with a diameter of 10 mm at one end and a 20 mm diameter at the other end, and then rolled at 723 K through a hole pattern in order to obtain transition tissues with different strain levels. The methodology employed to achieve a gradient structure was comprehensively described in our previous study [28]. Dynamic impact tests were conducted on samples with rolling reductions of 0%, 10%, 20%, and 30% (referred to as R0, R10, R20, and R30, respectively). A high-speed impact specimen shape of  $\varnothing 8 \text{ mm} \times 5 \text{ mm}$  cylindrical specimen was used. These tests were performed utilizing a split Hopkinson bar testing setup (ARCHIMEDESALT 1000, ARCHIMEDES, Tianjin, China), with impact pressures set at 0.15 MPa, 0.2 MPa, 0.25 MPa, and 0.3 MPa, corresponding to strain rates of  $800 \text{ s}^{-1}$ ,  $1400 \text{ s}^{-1}$ ,  $2000 \text{ s}^{-1}$ , and  $2400 \text{ s}^{-1}$ , respectively.

For microstructural analysis, an optical microscope (OM, OLYCIA M3) and a scanning electron microscope (SEM, JSM-6510A, JEOL Ltd., Tokyo, Japan) were employed. The  $\Phi 3 \text{ mm}$  disk foils were carefully prepared by grinding and punching. Subsequently, the samples underwent electrolytic jet polishing and ion milling. Transmission electron microscope (TEM) analysis was conducted using a JEM2100F with an energy dispersive X-ray spectrometer (EDAX-TSL, JEOL Ltd., Tokyo, Japan). The electron backscatter diffraction (EBSD) samples were subjected to argon ion polishing using the Hitachi ImpluS400 system (Hitachi, Tokyo, Japan) and were characterized using an SEM equipped with an Oxford C-nanoprobe (Zeiss Gemini 300, Carl Zeiss, Jena, Germany). To ensure accurate acquisition of EBSD datasets, a scanning step of 0.8  $\mu\text{m}$  was implemented.

## 3. Results and Discussion

### 3.1. Microstructural Evolution

Figure 1a–d shows the OM of the four strain samples before impact, and Figure 1e–t illustrates the OM of the four AZ31 samples following impact at various strain rates. The evolution of the impacted samples can be categorized into four stages as the strain rate increased. (1) At a strain rate of  $800 \text{ s}^{-1}$ , a significant number of twins formed across all samples. (2) At a strain rate of  $1400 \text{ s}^{-1}$ , the previously formed deformation twins largely disappeared, and further impact led to grain size reduction. (3) At a strain rate of  $2000 \text{ s}^{-1}$ , the impacted specimen experienced further growth in grain size accompanied

by a noticeable rise in temperature. (4) At a strain rate of  $2400\text{ s}^{-1}$ , all samples underwent fracture, characterized by a prominent presence of adiabatic shear bands and deformation twins within the sample. Clearly, the extent of temperature rise was positively correlated with the magnitude of the strain rate [16,29,30], which, in turn, allowed for the coarsening of the grain size to be imaged.

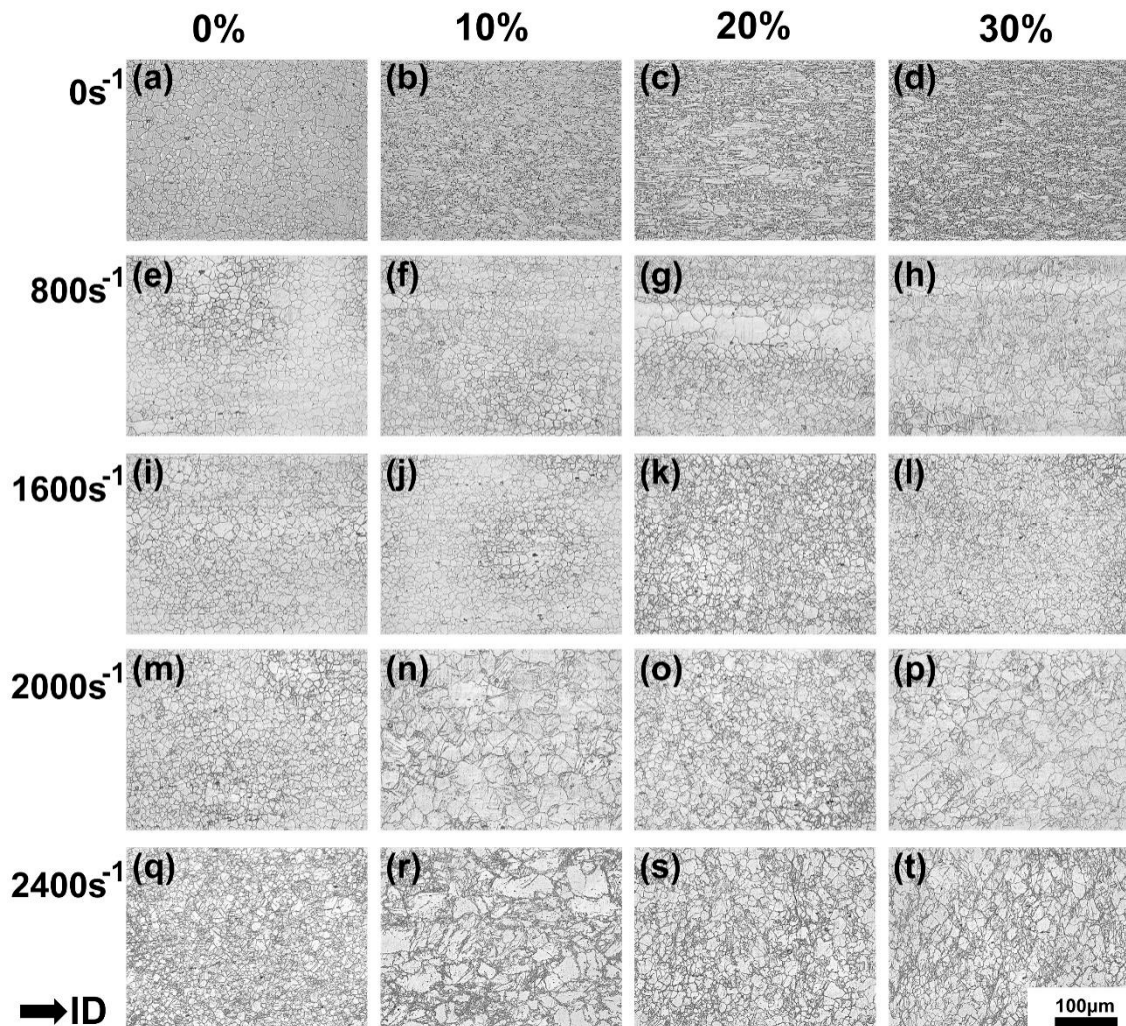


**Figure 1.** OM of AZ31 alloys with different rolling reductions of 0%, 10%, 20%, and 30% under different strain rates: (a–d) initial state, (e–h)  $800\text{ s}^{-1}$ , (i–l)  $1600\text{ s}^{-1}$ , (m–p)  $2000\text{ s}^{-1}$ , and (q–t)  $2400\text{ s}^{-1}$ . ID: impact direction.

Figure 2a–d presents the inverse pole figure (IPF) and grain size distribution diagram of samples that underwent different rolling reductions after impact at a strain rate of  $2000\text{ s}^{-1}$ . The impact-induced grain structure of the R0 and R30 samples appeared relatively uniform, while the R10 and R20 samples exhibited significant variation in grain size. In particular, the maximum grain size observed in the R10 sample was approximately 14.5 times larger than the average grain size (AGS). This discrepancy can be attributed to two factors. On one hand, the short impact deformation time resulted in some grains failing to promptly coordinate deformation, leading to significant disparities in grain distribution. On the other hand, the initial grain homogeneity also influenced this phenomenon. It is important to highlight that irrespective of the AGS before impact deformation, the AGS of each sample converged to around  $9\text{ }\mu\text{m}$  after impact at a strain rate of  $2000\text{ s}^{-1}$ . Even when the morphology varied considerably among all samples, the impact-induced deformation facilitated the formation of numerous fine grains within the coarse grains, enabling coordinated deformation and

a remarkable reduction in AGS. These findings align with observations from previous dynamic impact studies on Mg alloys [31–33].

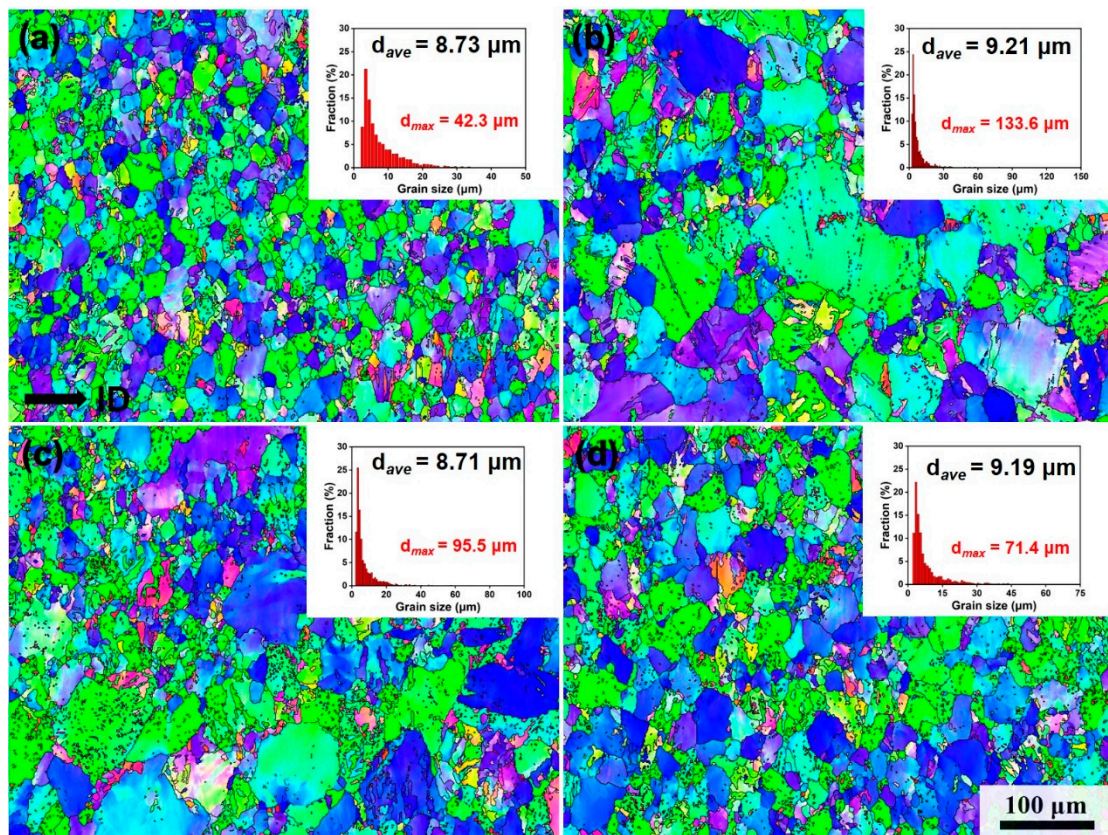


**Figure 2.** IPF and grain size distribution of AZ31 alloys with various rolling reductions after impact at a strain rate of  $2000 \text{ s}^{-1}$ : (a) 0%; (b) 10%; (c) 20%; and (d) 30%. ID: impact direction.

Figure 3 shows the texture distribution of the samples after impact at a strain rate of  $2000 \text{ s}^{-1}$ . There were no significant variations in texture intensity. The (0001) pole figure (PF) demonstrated a predominantly parallel distribution in relation to the impact direction (ID). Additionally, an IPF revealed the formation of a non-fiber texture component that was roughly parallel to the transverse direction (TD). In addition, the texture components were also detected in transitional orientations between the  $[10\text{-}10] \parallel \text{TD}$  and  $[11\text{-}20] \parallel \text{TD}$ .

When the Mg alloy was impacted at high speed, a considerable number of deformed grains were formed to accommodate the severe deformation [34]. Figure 4 presents the distribution and proportion of grains below the AGS in the impacted samples, along with their corresponding textures. The volume fraction ( $V_f$ ) of grains below the AGS was approximately 13%, and a highly uneven grain distribution was found due to more unbroken coarse grains when compared with Figure 2. Wang et al. [35] observed that when the compression direction (CD) aligns with the rolling direction (RD), the texture is enhanced. Conversely, when the CD is perpendicular to the RD, the texture becomes weaker.

The corresponding (0001) PF revealed that while certain grains maintained an orientation in which the c-axis was parallel to the impact direction (ID), most grains tended to diffuse along the normal direction (ND) and formed orientations offset by about  $30^\circ$  in the transverse direction (TD). The color distribution in the figure shows that the texture formed after impact became more pronounced as the rolling reduction increased. Weak texture components were observed in the R0 and R10 samples, while the R20 and R30 specimens exhibited distinct base poles. This illustrates that when the two deformations shared the same direction, the deformation during the initial process also influenced the texture generated by the subsequent deformation.

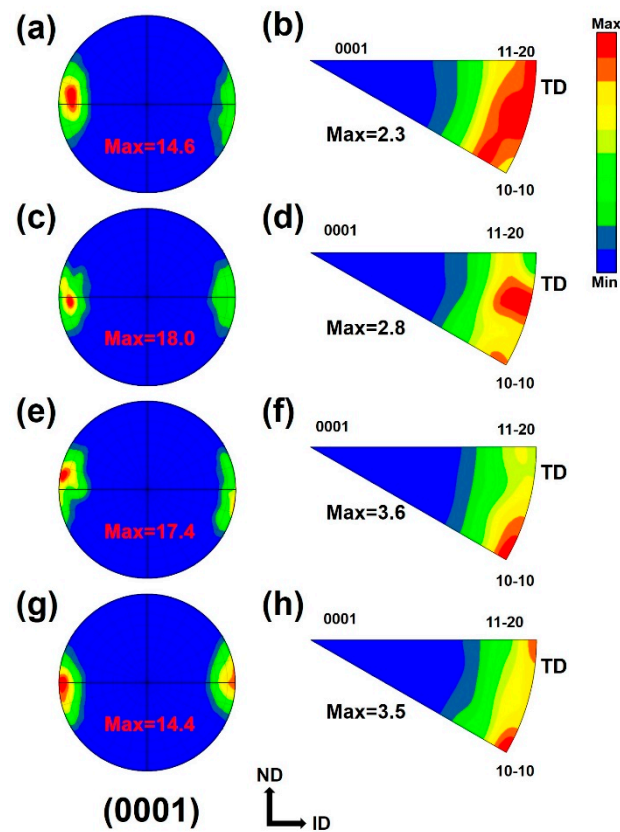


**Figure 3.** (a,c,e,g) (0001) PF and (b,d,f,h) IPF of specimens with different reductions (0%, 10%, 20%, and 30%) after impact at a strain rate of  $2000 \text{ s}^{-1}$ , respectively.

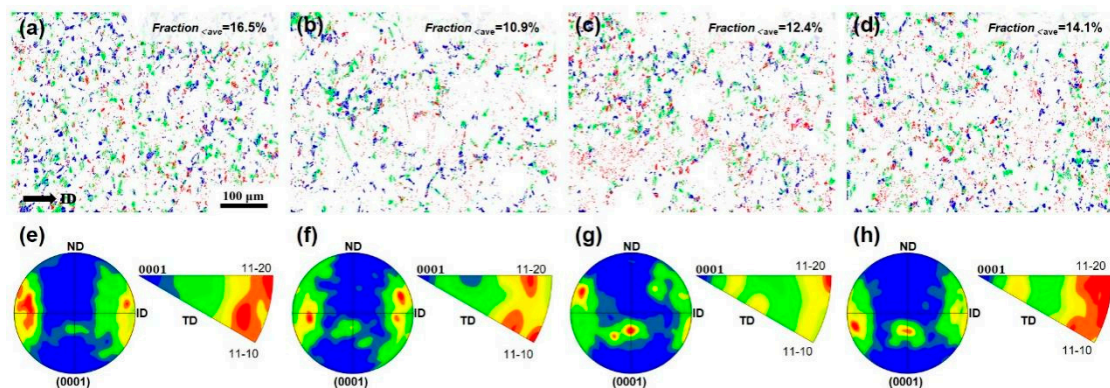


**Figure 4.** (a–d) IPF and proportion of the area with grain size below AGS after impact of the samples with deformation of 0%, 10%, 20%, and 30% at a strain rate of  $2000 \text{ s}^{-1}$  and (e–h) corresponding texture.

Generally, the deformation twins observed at high strain rates directly contribute to an increase in the average orientation difference (known as KAM), as depicted in Figure 5. The impacted samples displayed remarkably high KAM values, and the distribution of KAM within the coarse grains exhibited notable heterogeneity [36,37]. This phenomenon can be attributed to two factors: (1) The very short impact process limited the ability of some coarse grains to promptly undergo coordinated deformation. As a result, a nonuniform strain emerged within these grains. (2) A multitude of small grains involving dynamic recrystallization (DRX) formed within the coarse grains subsequent to impact. These newly formed grains exhibited relatively low KAM values and actively contributed to coordinating and influencing the KAM distribution to a significant extent. A similar finding was observed by Deng et al. [38], who proposed that twinning promotes the generation of

slip to further achieve coordinated deformation. Thus, a substantial number of twins were indeed produced during the impact process to facilitate coordinated deformation, resulting in a reduction in the AGS.

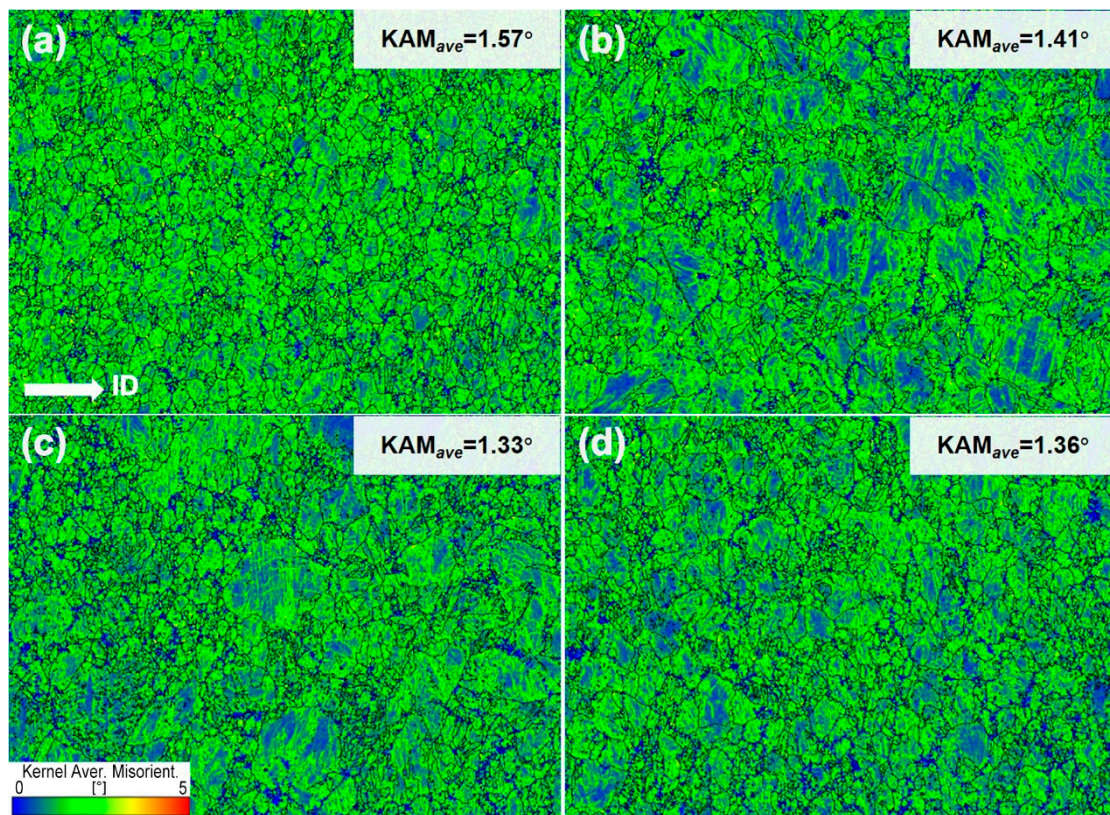


**Figure 5.** KAM distribution and average KAM values of samples with various rolling reductions after impact at a strain rate of  $2000 \text{ s}^{-1}$ : (a) 0%; (b) 10%; (c) 20%; and (d) 30%.

In addition, the microstructure of the samples after impact predominantly contained tensile twins, while compression twins and double twins were nearly absent. These tensile twins were primarily observed within the coarse grains, which highlights that tensile twins dominated the initial twinning deformation at high strain rates, as suggested by Chen et al. [39]. Figure 6 illustrates the specific distribution and  $V_f$  of the twins in specimen. For instance, in the case of the impact samples at a strain rate of  $2000 \text{ s}^{-1}$ , the R20 specimen exhibited the highest number of tensile twins, with a  $V_f$  of 23.4%. The formation of tensile twins mainly arose from certain original grains with basal texture. Additionally, due to the low critical resolved shear stress (CRSS) value associated with activating tensile twins, the strains corresponding to the impact deformation stage were fully sufficient to induce the highest number of tensile twins.

Comparing the IPF in Figure 2, nearly all the tensile twins form within the grains tended to exhibit a distribution aligned with the  $[11-20] \parallel \text{TD}$ , as illustrated in Figure 4. However, the actual orientation of the twins exhibited a noticeable deviation from this direction. As a result, the texture with a higher quantity of formed twins after impact significantly weakened in the  $[11-20] \parallel \text{TD}$ . Furthermore, it is notable that in Figure 4e, no non-fiber texture parallel to the TD formed. Gao et al. [40] also discovered that twins not only reduce the intensity of the texture but also alter the type of texture. In addition, the formation of numerous tensile twins within specific coarse grains largely affected the neighboring grain orientations. To conduct a comprehensive analysis, we focused on grains within two typical designated green rectangular frames, as depicted in Figure 6. The details are presented in Figure 7, using “P” to denote the parent grain and “ETs” to represent the tensile twins.

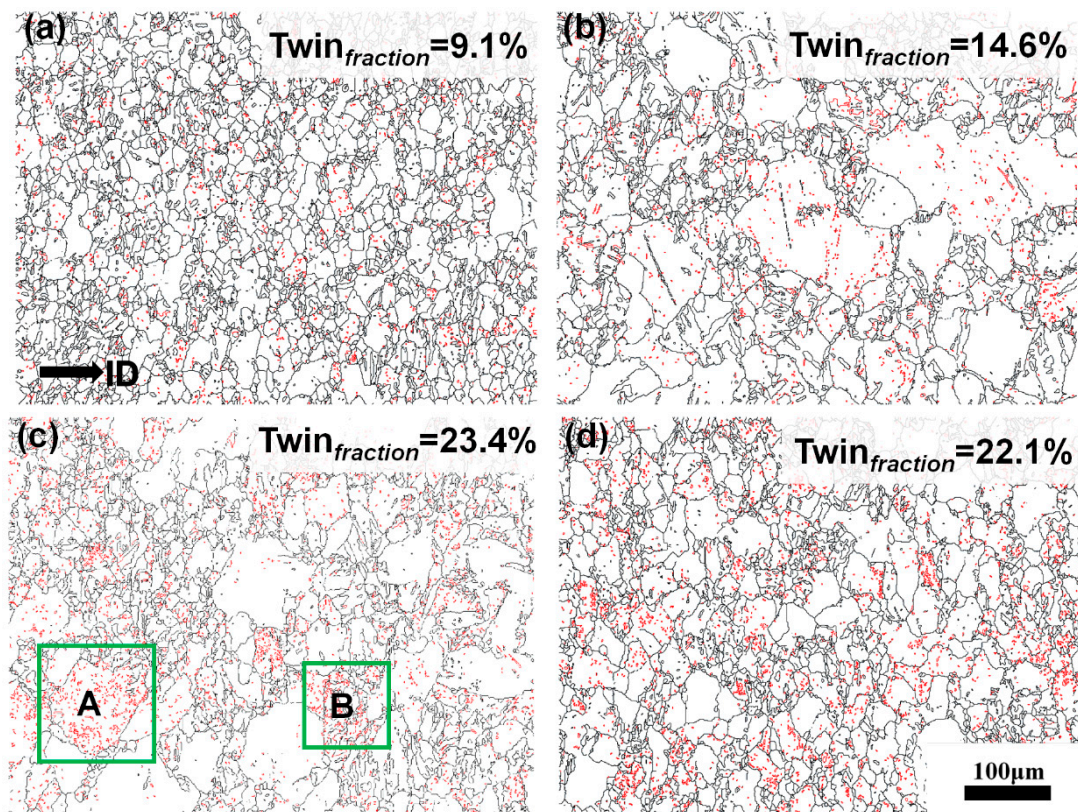


Figure 6. Twin distribution and its fraction with different rolling reductions after impact at a strain rate of  $2000 \text{ s}^{-1}$ : (a) 0%; (b) 10%; (c) 20%; and (d) 30%.

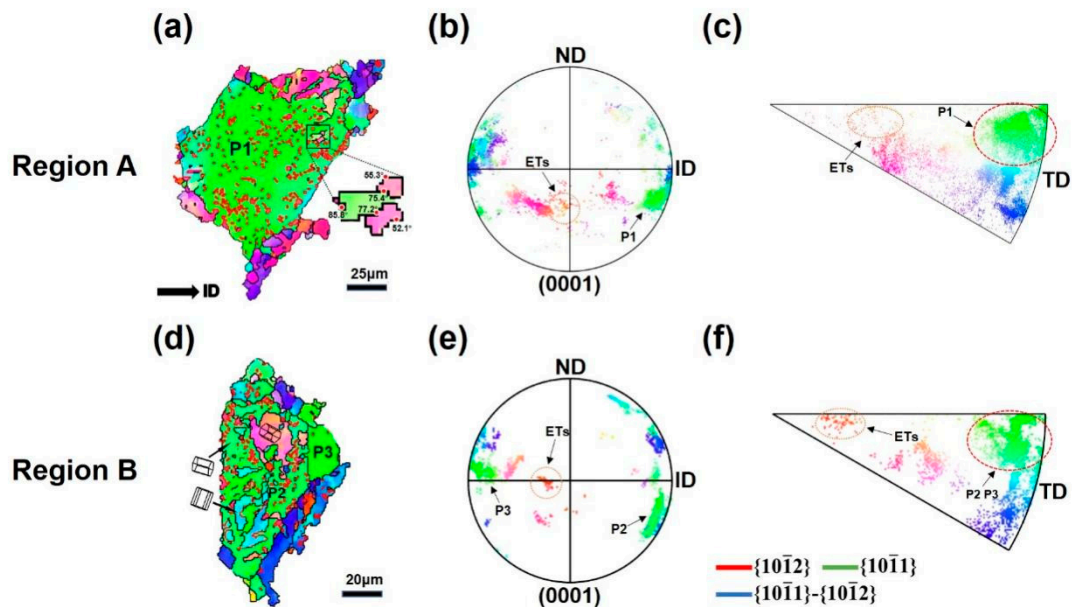


Figure 7. The EBSD result of the green rectangular box region in Figure 6 (c): (a,d) enlarged grains, and (b,e) and (c,f) correspond to (0001) PF and IPF, respectively.

In region A, a considerable number of tensile twins were observed within the P1 grains, and their orientations were generally consistent with the grains below the AGS. The corresponding texture components were formed near a  $30^\circ$  deviation from the ND to the TD in the (0001) PF. Conversely, the orientations of the grains surrounding P1 differed significantly from P1 itself. Some grains exhibited texture components similar to those

of the tensile twins, while others aligned with the  $[10\text{-}10] \parallel \text{TD}$ . Particularly, the black rectangular frame in Figure 7a revealed compelling evidence of the influence of tensile twins on the orientation of surrounding grains. A discernible gradient trend was observed in the grain boundary (GB) orientation difference among the three small grains formed adjacent to the twins. Moreover, the colors of these grains underwent significant changes. These observations further emphasize that the formation of tensile twins substantially impacts the orientation changes of the surrounding grains [41,42].

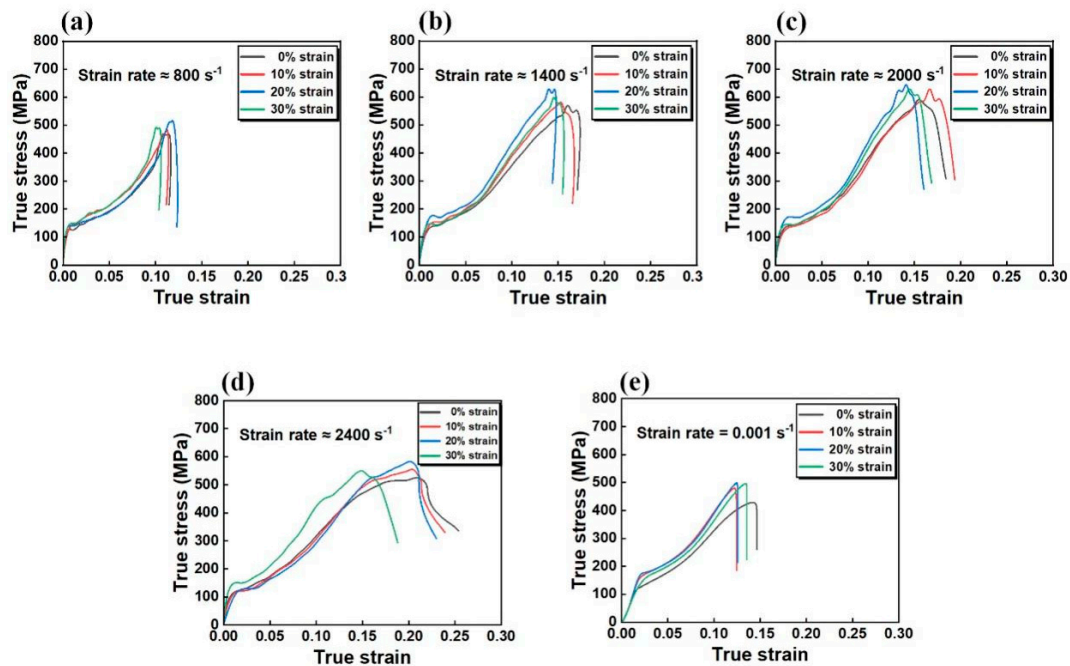
In region B, a number of tensile twins were also formed within the P2 and P3 grains. However, unlike the twins in region A, only a few grains surrounding the parent grains of these twins exhibited similar orientations. The texture orientations of the majority of the grains aligned with the  $[10\text{-}10] \parallel \text{TD}$ , with only a small number of grains sharing a similar orientation to their parent grains. Notably, it is important to highlight that grains with significantly different orientations formed at higher twin densities within the P2 grains. The texture orientations of the small grains formed around these grains closely resembled their own orientations, differing from the P2 grains. These observations indirectly indicate a notable influence of the formation of tensile twins on the texture components of the surrounding grains.

### 3.2. Mechanical Property

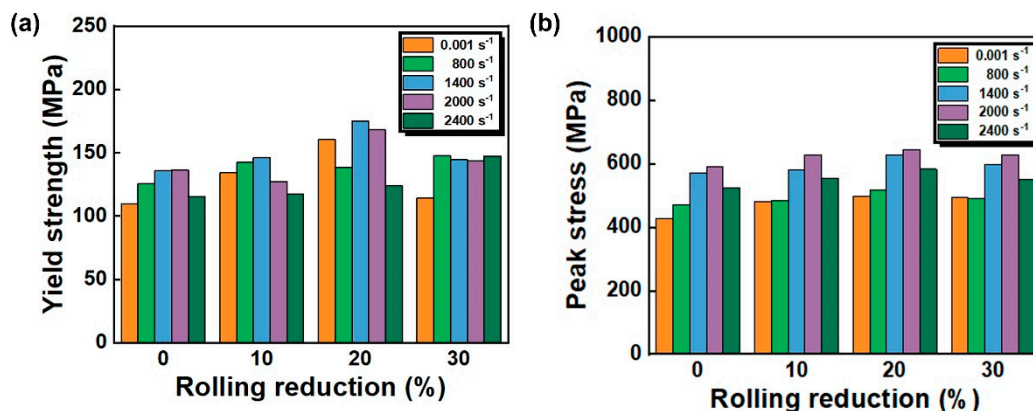
Figure 8 presents the true strain–stress curves of the gradient rolling samples with varying deformations after impact at different strain rates. All curves exhibited an S-shaped plot, which is characteristic of the twinning-dominated deformation mechanism in Mg alloys [43]. This kind of deformation process can be divided into three stages. Initially, during the early stage of impact, the alloy undergoes significant work hardening, with the stress rapidly increasing as strain accumulates. Once a certain threshold of strain is reached, a distinct yield platform becomes evident, and the stress exhibits a gradual upward trend. The presence of a low-yield platform arises from the loading direction induced by impact, favoring the formation of tensile twins in the initial stages of deformation. The relatively low CRSS required for tensile twin formation allows the material to adjust its deformation by generating such twins, leading to an earlier attainment of the yield condition. As deformation progresses further, the stress continues to rise, but the material experiences a competition between strain hardening and an adiabatic temperature rise associated with deformation at high strain rates. This competition results in fluctuations in the curve, leading to an oscillating behavior [44], and the stress reaches its peak value. Subsequently, the stress gradually decreases until deformation ceases. Figure 8e represents the true strain–stress curve under quasi-static compression. It can be observed that the shape of the curve is similar to those in Figure 8a–d, but the fluctuation region at the peak is absent, which indicates that there was no pronounced adiabatic temperature rise. Additionally, the peak stress was reduced, suggesting that higher strain rates contribute to work hardening.

Figure 9 illustrates the yield strength (YS) and peak compressive strength (CS) of all specimens in Figure 8. The R20 sample exhibited a higher YS compared to the other samples. Specifically, at a strain rate of  $1400 \text{ s}^{-1}$ , the YS of the R20 sample reached 175 MPa, surpassing the YS of the R0 sample at a strain rate of  $0.001 \text{ s}^{-1}$  by 65 MPa. In the case of the peak CS within the range from  $0.001 \text{ s}^{-1}$  to  $2000 \text{ s}^{-1}$ , the CS increased with higher strain rates. However, the impacted samples fractured when the strain rate reached  $2400 \text{ s}^{-1}$ , resulting in a significant decline in CS. Notably, the R20 sample consistently exhibited the highest CS across all strain rates. For example, the CS reached 644 MPa at a strain rate of  $2000 \text{ s}^{-1}$ , exceeding the CS of the same strain sample at a strain rate of  $0.001 \text{ s}^{-1}$  by 145 MPa. This also emphasizes the pronounced sensitivity of the CS of the impacted samples to the strain rate [30,45].





**Figure 8.** The true strain–stress curves of gradient rolling AZ31 alloys with different rolling reductions at strain rates of (a)  $800 \text{ s}^{-1}$ ; (b)  $1400 \text{ s}^{-1}$ ; (c)  $2000 \text{ s}^{-1}$ ; (d)  $2400 \text{ s}^{-1}$ ; and (e)  $0.001 \text{ s}^{-1}$ .



**Figure 9.** Summary of mechanical properties of all samples with different rolling reductions at various strain rates: (a) yield strength and (b) compressive strength.

Generally, the mechanical properties can be strengthened by solid solution strengthening, grain boundary strengthening, dislocation strengthening, and shear band strengthening [46–49]. TEM analysis was carried out for a better understanding of such strengthening mechanisms. Figure 10a displays the formation of high-density dislocations in the samples after impact (which agrees with Figure 5), demonstrating numerous dislocations at high strain rates using KAM analysis. Furthermore, the presence of layered structures in the dislocation region (see Figure 10b) and lattice distortions in the high-resolution image (see Figure 10c) confirm the existence of stacking faults (SFs) resulting from the interaction between SFs and a large number of dislocations. This interaction severely hindered the plastic deformation process, thereby improving the YS [50,51]. Additionally, a twin–twin interaction was observed within the impact specimen (see Figure 10d,e), which also contributed to strengthening of the AZ31 alloy. In addition to dislocations and twinning, Figure 10g reveals the presence of numerous nanoscale second-phase particles and some DRXed grains. Detailed EDS mapping indicated that these second particles were in the Al–Mn phases. Most of these particles were located near dislocations and hindered the movement of dislocations to some extent, thus enhancing these properties as well. In

addition, in light of Figure 2, which exhibited lots of fine grains, a decrease in grain size by DRX enhanced the YS according to the well-known Hall–Petch equation. In the case of quasi-static compression at low strain rates, the YS and CS of as-rolled samples remained low. However, when the strain rate reached a medium level and the sample still did not fracture after impact, both the YS and CS increased significantly (i.e., R20 sample). When the strain rate reached a high enough level that it caused specimen failure, the corresponding strength decreased dramatically, and the alloy exhibited negative strain rate sensitivity [52].

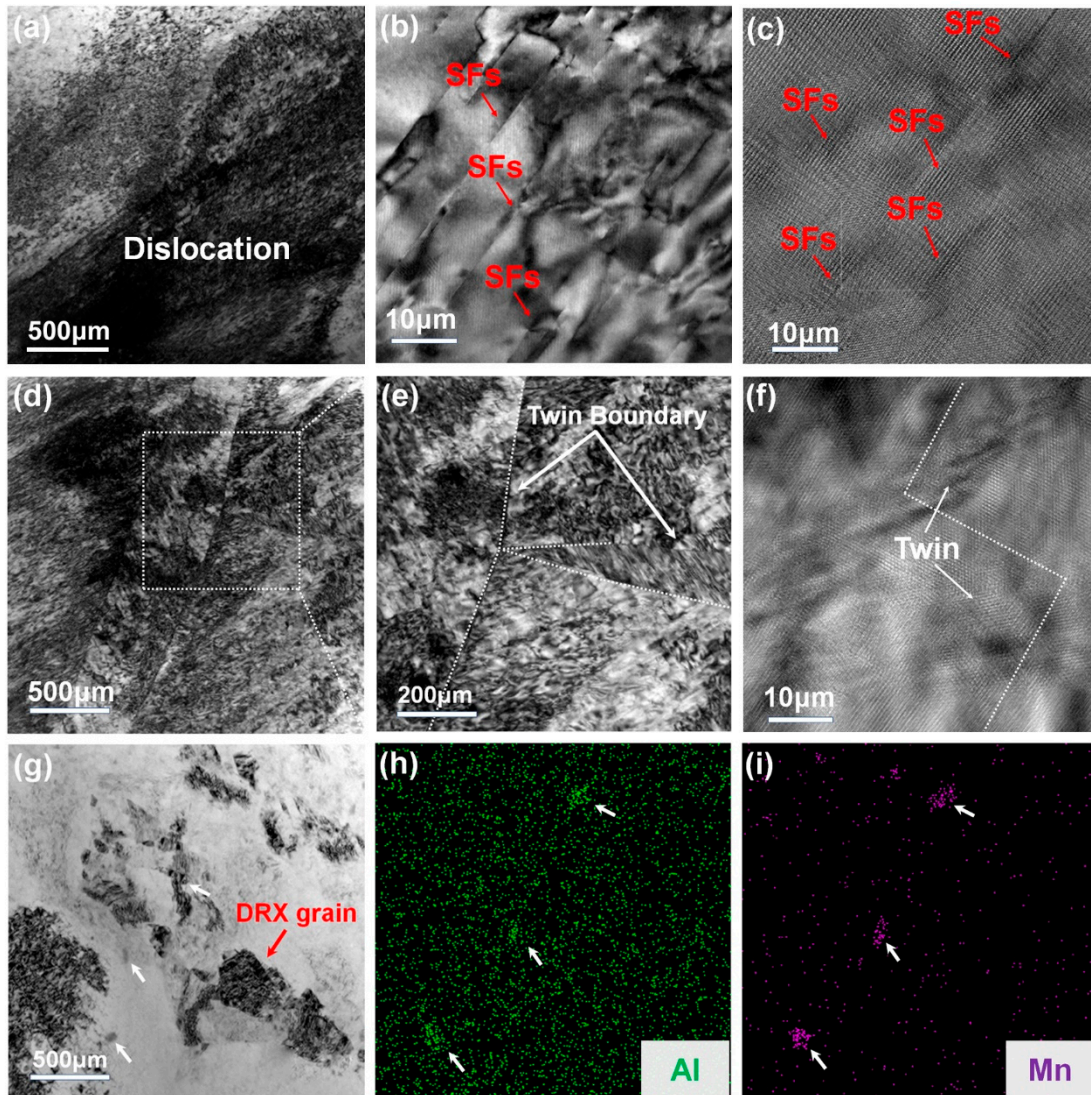


**Figure 10.** TEM of the sample with 20% rolling reduction after impact at a strain rate of  $2000 \text{ s}^{-1}$ : (a,b,d,e,g) bright-field image of defects and substructure; (c,f) high-resolution image corresponding to (b,e); and (h,i) EDS mapping of (g).

Figure 11 illustrates the Vickers hardness of AZ31 alloys subjected to different rolling reductions after impact. By examining the OM presented in Figure 1 and correlating it with these hardness values, it became apparent that the hardness values of all samples increased significantly with higher strain rates. However, at strain rates of  $1400 \text{ s}^{-1}$ ,  $2000 \text{ s}^{-1}$ , and  $2400 \text{ s}^{-1}$ , the hardness values did not exhibit a positive strain rate sensitivity. Specifically, both the R0 and R30 samples consistently exhibited hardness values of approximately 70 HV after impact. In contrast, the hardness values of the R10 and R20 samples demonstrated a negative strain rate sensitivity with an increase in strain rate from  $1400 \text{ s}^{-1}$  to  $2000 \text{ s}^{-1}$ . This phenomenon was attributed to the significant increase in grain size observed in the

R10 and R20 samples following impact at a strain rate of  $2000\text{ s}^{-1}$ . It is noteworthy that despite all samples fracturing at a strain rate of  $2400\text{ s}^{-1}$ , the hardness measurement of the fractured sample indicates that the hardness value remained higher than the value prior to impact. This suggests that a substantial amount of deformation energy was absorbed by the sample prior to fracture/failure. Moreover, it is worth emphasizing that Figure 11 exhibits a significant hardness error bar for the R10 sample following impact at a strain rate of  $2400\text{ s}^{-1}$ . Correlating this with the OM shown in Figure 1n, it becomes evident that the microstructure of the sample became highly heterogeneous after impact, primarily due to the presence of numerous shear bands. These measurements further support the well-established Hall–Petch relationship between hardness and grain size [53].

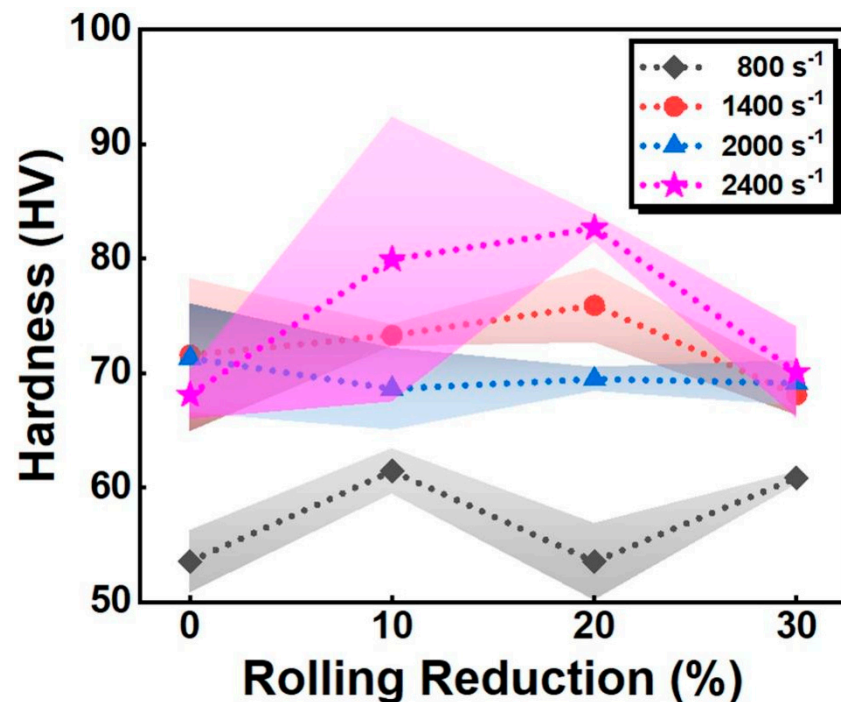


**Figure 11.** Vickers hardness of AZ31 alloys with different rolling reductions after impact at various strain rates.

Further examination of the shear band is presented in Figure 12. Although the grains within the shear band remained unevenly distributed, their size was significantly smaller compared to previous structures. Additionally, some nanocrystals and numerous nanoscale second phases in the shear band, as depicted in Figure 12b,d, contributed to the improved performance. However, at high strain rates, molten metal can be seen, as shown in Figure 12d (indicated by the red arrow), which, due to the local generation of heat during impact, resulted in limited heat dissipation and elevated temperatures within the shear band. Moreover, Figure 12b,d highlight the presence of micro-cracks surrounding specific grains, as indicated by the orange arrows. These micro-cracks have a tendency to propagate along adiabatic shear bands and can act as precursors to failure [54,55], providing an explanation for the fracture at the strain rate of  $2400\text{ s}^{-1}$ .

In summary, when the as-rolled AZ30 alloy was subjected to deformation at high strain rates, a substantial number of deformation twins were generated, leading to an increase in dislocation density and noticeable work hardening. Concurrently, shear bands formed as dislocations slipped along specific GBs, resulting in the accumulation and interaction of dislocations, thereby enhancing the final performance. Moreover, due to the limited dissipation of heat, there was a rapid rise in temperature during short impact, leading to grain recrystallization, the occurrence of molten metal, and enhanced work hardening. All these factors contributed to a reduction in the AGS and an improvement in the mechanical

properties. Additionally, the continued development of adiabatic shear bands was accompanied by the formation of cracks, which led to the failure and fragmentation of the alloys at excessively high strain rates.

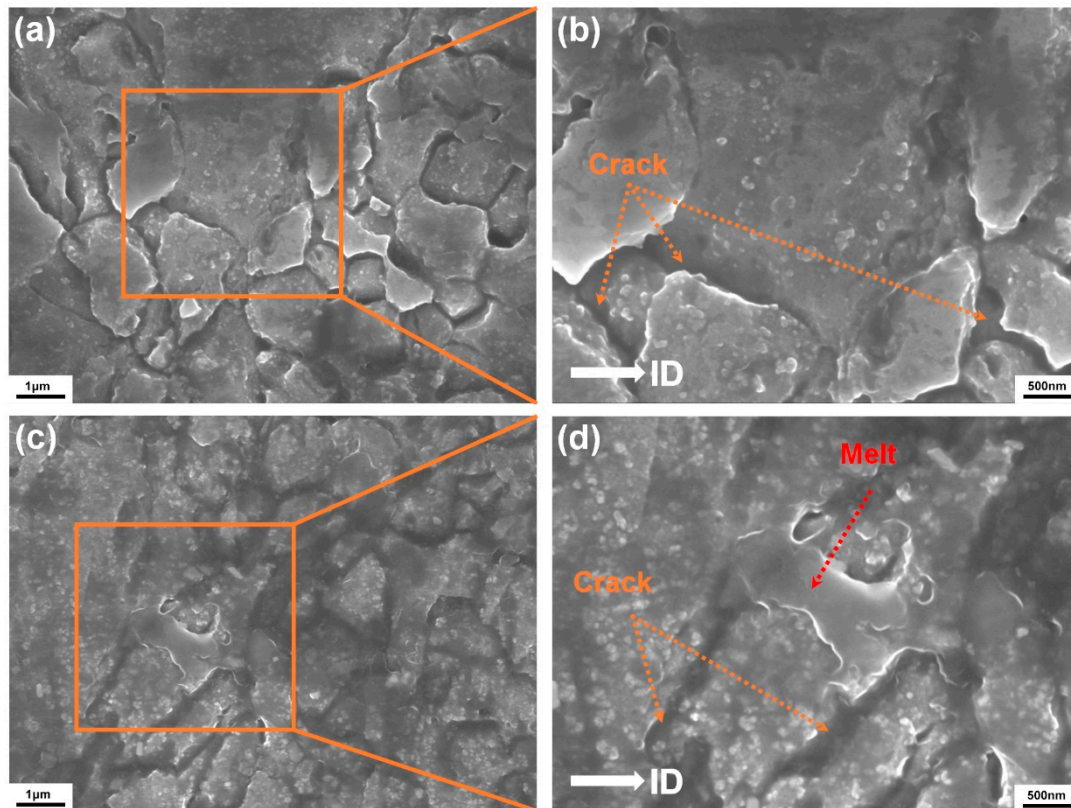


**Figure 12.** SEM morphology of adiabatic shear band: (a,c) SEM images inside the shear band; (b,d) are enlarged images of (a,c).

#### 4. Conclusions

In this study, we conducted a comprehensive investigation of the dynamic impact behavior of AZ31 alloys with different rolling reductions and subjected them to different strain rates. Based on the above analysis and discussion of the microstructure and mechanical properties, the following conclusions can be drawn. With an escalation in strain rate, the formation of twins promoted DRX, and the microstructure became heterogeneous. These twins showed a remarkable effect regarding the modification of the orientation of neighboring grains. Importantly, at very high strain rates, the specimens experienced fractures, resulting in the formation of numerous adiabatic shear bands and deformation twins. In addition, a positive strain rate sensitivity was observed in the mechanical properties of the specimens prior to fracture, with the 20% rolling reduction alloy exhibiting the highest strength at a strain rate of  $2000 \text{ s}^{-1}$ . This increase in strength was attributed primarily to the combined influence of grain refinement, numerous dislocation formations, and profuse precipitates.

**Author Contributions:** Conceptualization, F.Y. and H.Y.; methodology, H.Y., W.Y., Y.X., B.J., K.S. and F.Y.; writing—original draft preparation, Y.L. (Yingjie Li), H.Y. and C.L.; writing—review and editing, H.Y., C.L., W.Y., Y.X., B.J., K.S. and F.Y.; validation, Y.L. (Yingjie Li), Y.L. (Yu Liu), C.L. and W.Y.; investigation, Y.L. (Yingjie Li), H.Y., C.L., Y.L. (Yu Liu) and W.Y.; data curation, Y.L. (Yingjie Li), W.Y., Y.L. (Yu Liu), Y.X., B.J. and K.S.; project administration, H.Y. All authors have read and agreed to the published version of the manuscript.

**Funding:** This work was supported by the Natural Science Foundation of Hebei province (no. E2022202158) and the foundation of strengthening program (2019-JCJQ-142-00).

**Data Availability Statement:** The raw/processed data required to reproduce these findings cannot be shared at this time, as the data are part of an ongoing study.

**Conflicts of Interest:** Author Yuling Xu was employed by the company Baosteel Metal Co., Ltd. The remaining authors declare that the research was conducted in the absence of any commercial or financial relationships that could be construed as a potential conflict of interest.

## References

- Zhao, Y.; Dong, G.; Zhao, B. Research progress of magnesium alloy application in aviation manufacturing. *Nonferrous Met. Eng.* **2015**, *5*, 23–27.
- Yu, K.; Li, W.; Ma, Z. Research, development and application of wrought magnesium alloys. *Chin. J. Nonferrous Met.* **2003**, *13*, 277–288.
- Yang, Y.; Li, J.; Song, H.; Liu, P. Application of Magnesium Alloys and Current Status of Their Forming Technology Research. *Hot Work. Technol.* **2013**, *42*, 24–27. (In Chinese)
- Wang, J.; Ju, J.; Huang, Z.; Shu, Y. Research Progress on Preparation Technology of Magnesium Alloy Sheet. *Hot Work. Technol.* **2014**, *43*, 6–9+5.
- Meng, R.; Zhang, D.; Yuan, H. Progress of Forming Technologies for Magnesium Alloy. *Hot Work. Technol.* **2008**, *37*, 89–92.
- Hou, Z.; Jiang, B.; Wang, Y.; Song, J.; Xiao, L.; Pan, F. Development and Application of New Magnesium Alloy Materials and their New Preparation and Processing Technologies. *Aerosp. Shanghai* **2021**, *38*, 119–133.
- Deng, H.; He, B. Research progress in fatigue properties of magnesium alloy welded joints. *Ordinance Mater. Sci. Eng.* **2016**, *39*, 125–129.
- Chen, W.; Zhan, M.; Chen, W.; Zhang, D.; Li, Y. Present Status of Plastic Working for Wrought Magnesium Alloy and Its Future. *Spec. Cast. Non-Ferr. Alloys* **2007**, *27*, 40–43.
- Bao, J.; Li, Q.A.; Chen, X.; Zhang, Q.; Chen, Z. Research Progress on Extruded Magnesium Alloys. *Mater. Rev.* **2022**, *36*, 20090073-12.
- Elambharathi, B.; Kumar, S.D.; Dhanoop, V.U.; Dinakar, S.; Rajumar, S.; Sharma, S.; Kumar, V.; Li, C.; Eldin, E.M.T.; Wojciechowski, S. Novel insights on different treatment of magnesium alloys: A critical review. *Heliyon* **2022**, *8*, e11712. [[CrossRef](#)]
- Che, B.; Lu, L.; Kang, W.; Luo, J.; Ma, M.; Liu, L. Hot deformation behavior and processing map of a new type Mg-6Zn-1Gd-1Er alloy. *J. Alloys Compd.* **2021**, *862*, 158700. [[CrossRef](#)]
- Figueiredo, R.B.; Langdon, T.G. Deformation mechanisms in ultrafine-grained metals with an emphasis on the Hall–Petch relationship and strain rate sensitivity. *J. Mater. Res. Technol.-JmrT* **2021**, *14*, 137–159. [[CrossRef](#)]
- Liu, Y.; Li, Y.; Zhu, Q.; Zhang, H.; Qi, X.; Wang, J.; Jin, P.; Zeng, X. Twin recrystallization mechanisms in a high strain rate compressed Mg-Zn alloy. *J. Magnes. Alloys* **2021**, *9*, 499–504. [[CrossRef](#)]
- Long, J.; Xia, Q.; Xiao, G.; Qin, Y.; Yuan, S. Flow characterization of magnesium alloy ZK61 during hot deformation with improved constitutive equations and using activation energy maps. *Int. J. Mech. Sci.* **2021**, *191*, 106069. [[CrossRef](#)]
- Malik, A.; Wang, Y.; Huanwu, C.; Nazeer, F.; Khan, M.A. Dynamic mechanical behavior of magnesium alloys: A review. *Int. J. Mater. Res.* **2019**, *110*, 1105–1115. [[CrossRef](#)]
- Malik, A.; Nazeer, F.; Naqvi, S.Z.H.; Long, J.; Li, C.; Yang, Z.; Huang, Y. Microstructure feathers and ASB susceptibility under dynamic compression and its correlation with the ballistic impact of Mg alloys. *J. Mater. Res. Technol.-JmrT* **2022**, *16*, 801–813. [[CrossRef](#)]
- Jin, Z.Z.; Cheng, X.M.; Zha, M.; Rong, J.; Zhang, H.; Wang, J.G.; Wang, C.; Li, Z.G.; Wang, H.Y. Effects of Mg17Al12 second phase particles on twinning-induced recrystallization behavior in Mg-Al-Zn alloys during gradient hot rolling. *J. Mater. Sci. Technol.* **2019**, *35*, 2017–2026. [[CrossRef](#)]
- Zhang, L.; Townsend, D.; Petrinic, N.; Pellegrino, A. Measurement of Pure Shear Constitutive Relationship From Torsion Tests Under Quasi-Static, Medium, and High Strain Rate Conditions. *J. Appl. Mech.-Trans. ASME* **2021**, *88*, 121003. [[CrossRef](#)]
- Zhou, S.; Deng, C.; Liu, S.; Liu, Y.; Zhu, J.; Yuan, X. Effect of strain rates on mechanical properties, microstructure and texture inside shear bands of pure magnesium. *Mater. Charact.* **2022**, *184*, 111686. [[CrossRef](#)]
- Chen, Z.; Li, Q.; Chen, X.; Zhu, H. Research Status and Application of Zn-Containing Magnesium Alloys and Influence of LPSO on Alloy Properties. *J. Chin. Soc. Rare Earths* **2021**, *39*, 860–870.
- Pan, H.; Ren, Y.; Fu, H.; Zhao, H.; Wang, L.; Meng, X.; Qin, G. Recent developments in rare-earth free wrought magnesium alloys having high strength: A review. *J. Alloys Compd.* **2016**, *663*, 321–331. [[CrossRef](#)]
- Su, Z.; Huang, Y.; Liu, C.; Yang, X. Progress in RE-containing Cast Magnesium Alloys. *Spec. Cast. Nonferrous Alloys* **2015**, *35*, 1047–1051.
- Cerreta, E.K.; Fensin, S.J.; Perez-Bergquist, S.J.; Trujillo, C.P.; Morrow, B.M.; Lopez, M.F.; Roach, C.J.; Mathaudhu, S.N.; Anghel, V.; Gray, G.T., III. The High-Strain-Rate Constitutive Behavior and Shear Response of Pure Magnesium and AZ31B Magnesium Alloy. *Metall. Mater. Trans. A-Phys. Metall. Mater. Sci.* **2021**, *52*, 3152–3170. [[CrossRef](#)]
- Liu, F.; Liu, X.; Zhu, B.; Yang, H.; Xiao, G.; Hu, M. Influence of Microstructure and Mechanical Properties on Formability in High Strain Rate Rolled AZ31 Magnesium Alloy Sheets. *Met. Mater. Int.* **2022**, *28*, 1361–1371. [[CrossRef](#)]

25. Liu, X.; Wan, Q.; Yang, H.; Zhu, B.; Wu, Y.; Liu, W.; Tang, C. The Effect of Twins on Mechanical Properties and Microstructural Evolution in AZ31 Magnesium Alloy during High Speed Impact Loading. *J. Mater. Eng. Perform.* **2022**, *31*, 3208–3217. [[CrossRef](#)]
26. Yu, J.; Dong, F.; Xu, N.; Chen, Y.; Mao, P.; Liu, Z. Dynamic compressive properties and microstructural evolution of EW75 magnesium alloy at high temperatures and high strain rates. *Chin. J. Rare Met.* **2019**, *43*, 141–150.
27. Ji, Y.-F.; Duan, J.-R.; Yuan, H.; Li, H.-Y.; Sun, J.; Ma, L.-F. Effect of variable thickness cross rolling on edge crack and microstructure gradient of AZ31 magnesium alloy. *J. Cent. South Univ.* **2022**, *29*, 1124–1132. [[CrossRef](#)]
28. Yu, H.; Wang, D.; Liu, Y.; Liu, Y.; Huang, L.; Jiang, B.; Park, S.; Yu, W.; Yin, F. Recrystallization mechanisms and texture evolution of AZ31 alloy by gradient caliber rolling. *J. Mater. Res. Technol.* **2023**, *23*, 611–626. [[CrossRef](#)]
29. Guo, P.; Tang, Q.; Li, L.; Xie, C.; Liu, W.; Zhu, B.; Liu, X. The deformation mechanism and adiabatic shearing behavior of extruded Mg-8.0Al-0.1Mn alloy in different heat treated states under high-speed impact load. *J. Mater. Res. Technol.-JmrT* **2021**, *11*, 2195–2207. [[CrossRef](#)]
30. Li, Q. Mechanical properties and microscopic deformation mechanism of polycrystalline magnesium under high-strain-rate compressive loadings. *Mater. Sci. Eng. A-Struct. Mater. Prop. Microstruct. Process.* **2012**, *540*, 130–134. [[CrossRef](#)]
31. Zhu, B.; Liu, X.; Xie, C.; Liu, W.; Tang, C.; Lu, L. The flow behavior in as-extruded AZ31 magnesium alloy under impact loading. *J. Magnes. Alloys* **2018**, *6*, 180–188. [[CrossRef](#)]
32. Nazeer, F.; Naqvi, S.Z.H.; Kalam, A.; Al-Sehemi, A.G.; Alrobei, H. Texture dependencies on flow stress behavior of magnesium alloy under dynamic compressive loading. *Vacuum* **2021**, *191*, 110323. [[CrossRef](#)]
33. Tang, W.; Liu, S.; Liu, Z.; Kang, S.; Mao, P.; Zhou, L.; Wang, Z. Microstructure evolution and constitutive relation establishment of Mg-7Gd-5Y-1.2Nd-0.5Zr alloy under high strain rate after severe multi-directional deformation. *Mater. Sci. Eng. A-Struct. Mater. Prop. Microstruct. Process.* **2021**, *809*, 140994. [[CrossRef](#)]
34. Du, Y.; Du, W.; Zhang, D.; Ge, Y.; Jiang, B. Enhancing mechanical properties of an Mg-Zn-Ca alloy via extrusion. *Mater. Sci. Technol.* **2021**, *37*, 624–631. [[CrossRef](#)]
35. Wang, Q.; Zhai, H.; Xia, H.; Liu, L.; He, J.; Xia, D.; Yang, H.; Jiang, B. Relating Initial Texture to Deformation Behavior During Cold Rolling and Static Recrystallization Upon Subsequent Annealing of an Extruded WE43 Alloy. *Acta Metall. Sin.-Engl. Lett.* **2022**, *35*, 1793–1811. [[CrossRef](#)]
36. Xu, Y.; Yin, K.; Xia, L.; Chen, S.; Men, X.; Deng, T.; Wang, Y.; Zhang, S.-H. Study on High-Speed Tensile Mechanical Properties and Deformation Mechanism of 2195 Al-Li Alloy Sheet. *Rare Met. Mater. Eng.* **2022**, *51*, 1283–1292.
37. Liu, J.; Lu, L.; Zhong, Z. Deformation twins and annealing twins in high purity coarse-grained aluminum by equal channel angular pressing at high strain rate. *J. Mater. Eng.* **2021**, *49*, 89–94.
38. Deng, J.-F.; Tian, J.; Zhou, Y.; Chang, Y.; Liang, W.; Ma, J. Plastic deformation and fracture mechanisms of rolled Mg-8Gd-4Y-Zn and AZ31 magnesium alloys. *Mater. Des.* **2022**, *223*, 111179. [[CrossRef](#)]
39. Chen, Y.; Mao, P.; Wang, Z.; Cao, G. Tensile twin evolution of Mg-3Al-1Zn magnesium alloy during high-strain rate deformation. *Mater. Sci. Technol.* **2021**, *37*, 1452–1464. [[CrossRef](#)]
40. Gui, Y.; Cui, Y.; Bian, H.; Li, Q.; Ouyang, L.; Chiba, A. Role of slip and {10-12} twin on the crystal plasticity in Mg-RE alloy during deformation process at room temperature. *J. Mater. Sci. Technol.* **2021**, *80*, 279–296. [[CrossRef](#)]
41. Han, X.; Xiao, T.; Yu, Z. Microstructure, Texture Evolution, and Strain Hardening Behaviour of As-extruded Mg-Zn and Mg-Y Alloys under Compression. *J. Wuhan Univ. Technol.-Mater. Sci. Ed.* **2023**, *38*, 430–439. [[CrossRef](#)]
42. Deng, G.; Li, A.; Li, W.; Chang, G.; Liu, Y. Deformation Mechanism and Microstructural Evolution of a Mg-Y-Nd-Zr Alloy under High Strain Rate at Room Temperature. *J. Mater. Eng. Perform.* **2023**, *33*, 3101–3114. [[CrossRef](#)]
43. Dixit, N.; Xie, K.Y.; Hemker, K.J.; Ramesh, K.T. Microstructural evolution of pure magnesium under high strain rate loading. *Acta Mater.* **2015**, *87*, 56–67. [[CrossRef](#)]
44. Yang, Y.; He, J.; Huang, J.; Lian, X. Difference in adiabatic shear susceptibility between pure copper and Cu-30% Zn solid solution alloy at different strain rate. *J. Mater. Res.* **2023**, *38*, 1410–1419. [[CrossRef](#)]
45. Liu, X.Y.; Pan, Q.L.; He, Y.B.; Li, W.B.; Liang, W.J.; Yin, Z.M. Flow behavior and microstructural evolution of Al-Cu-Mg-Ag alloy during hot compression deformation. *Mater. Sci. Eng. A-Struct. Mater. Prop. Microstruct. Process.* **2009**, *500*, 150–154. [[CrossRef](#)]
46. Wei, Q.; Yuan, L.; Shan, D.; Guo, B. Study on the microstructure and mechanical properties of ZK60 magnesium alloy with submicron twins and precipitates obtained by room temperature multi-directional forging. *J. Mater. Sci.* **2023**, *58*, 13236–13250. [[CrossRef](#)]
47. Mottaghian, F.; Taheri, F. Strength and failure mechanism of single-lap magnesium-basalt fiber metal laminate adhesively bonded joints: Experimental and numerical assessments. *J. Compos. Mater.* **2022**, *56*, 1941–1955. [[CrossRef](#)] [[PubMed](#)]
48. Liu, Z.; Wu, F.; Feng, B.; Liu, L.; Dong, C.; Zhao, Y.; Song, B. Enhancing mechanical properties of friction stir welded AZ31 alloys by post-weld compression. *Sci. Technol. Weld. Join.* **2023**, *28*, 468–477. [[CrossRef](#)]
49. Ding, N.; Du, W.; Zhu, X.; Dou, L.; Wang, Y.; Li, X.; Liu, K.; Li, S. Roles of LPSO phases on dynamic recrystallization of high strain rate multi-directional free forged Mg-Gd-Er-Zn-Zr alloy and its strengthening mechanisms. *Mater. Sci. Eng. A-Struct. Mater. Prop. Microstruct. Process.* **2023**, *864*, 144590. [[CrossRef](#)]
50. Alaneme, K.K.; Okotete, E.A. Enhancing plastic deformability of Mg and its alloys—A review of traditional and nascent developments. *J. Magnes. Alloys* **2017**, *5*, 460–475. [[CrossRef](#)]
51. Zhu, S.Q.; Ringer, S.P. On the role of twinning and stacking faults on the crystal plasticity and grain refinement in magnesium alloys. *Acta Mater.* **2018**, *144*, 365–375. [[CrossRef](#)]

52. Tan, L.; Huang, X.; Wang, Y.; Sun, Q.; Zhang, Y.; Tu, J.; Zhou, Z. Activation Behavior of {10-12}-{10-12} Secondary Twins by Different Strain Variables and Different Loading Directions during Fatigue Deformation of AZ31 Magnesium Alloy. *Metals* **2022**, *12*, 1433. [[CrossRef](#)]
53. Doiphode, R.L.; Murty, S.V.S.N.; Prabhu, N.; Kashyap, B.P. Grain growth in calibre rolled Mg–3Al–1Zn alloy and its effect on hardness. *J. Magnes. Alloys* **2015**, *3*, 322–329. [[CrossRef](#)]
54. Pedersen, K.O.; Borvik, T.; Hopperstad, O.S. Fracture mechanisms of aluminium alloy AA7075-T651 under various loading conditions. *Mater. Des.* **2011**, *32*, 97–107. [[CrossRef](#)]
55. Zou, D.L.; Zhen, L.; Zhu, Y.; Xu, C.Y.; Shao, W.Z.; Pang, B.J. Deformed microstructure evolution in AM60B Mg alloy under hypervelocity impact at a velocity of 5 kms<sup>-1</sup>. *Mater. Des.* **2010**, *31*, 3708–3715. [[CrossRef](#)]

**Disclaimer/Publisher’s Note:** The statements, opinions and data contained in all publications are solely those of the individual author(s) and contributor(s) and not of MDPI and/or the editor(s). MDPI and/or the editor(s) disclaim responsibility for any injury to people or property resulting from any ideas, methods, instructions or products referred to in the content.